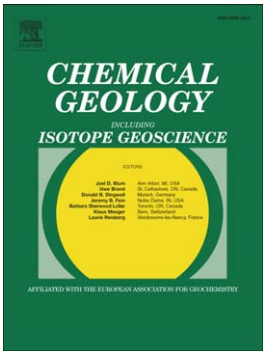

Growth-rate induced disequilibrium of oxygen isotopes in aragonite: An in situ study

Rinat I. Gabitov

PII: S0009-2541(13)00221-0
DOI: doi: 10.1016/j.chemgeo.2013.05.015
Reference: CHEMGE 16885

To appear in: *Chemical Geology*

Received date: 25 December 2012
Revised date: 30 April 2013
Accepted date: 15 May 2013

Please cite this article as: Gabitov, Rinat I., Growth-rate induced disequilibrium of oxygen isotopes in aragonite: An in situ study, *Chemical Geology* (2013), doi: 10.1016/j.chemgeo.2013.05.015

Growth-rate induced disequilibrium of oxygen isotopes in aragonite: An in situ study.

Rinat I. Gabitov

Department of Geosciences, Mississippi State University, MS, 39762-5448

Email: rinat.gabitov@gmail.com

Abstract

Oxygen isotope compositions ($\delta^{18}O$) of biogenic and inorganically precipitated calcium carbonate minerals are being used to reveal marine and terrestrial temperatures from the past. However, experimental and natural observations show factors other than temperature control $\delta^{18}O$ in $CaCO_3$ via disequilibrium fractionation. Crystallization rate is among these factors, and therefore, its effect on fractionation process has been studied during the last 30 years. However, most previous experimental assessments measured $\delta^{18}O$ in polycrystalline precipitates using bulk analytical techniques and defined growth rate as the total amount of $CaCO_3$ crystallized during the period of time. Because of this, inter- and intra-crystal isotopic variability has remained poorly constrained. In order to evaluate the effect of crystal extension rate (V) on ^{18}O fractionation between aragonite and fluid an alternative analytical approach was used. Hemispherical bundles of aragonite crystals (spherulites) were measured for $\delta^{18}O$ *in situ* with Secondary Ion Mass Spectrometry (SIMS) at lateral spatial resolution of 10-20 μm. The change in V over time was monitored by addition of multiple rare earth element (REE) spikes into the fluid from which the aragonite grew. $\delta^{18}O$ in fluid were analyzed with stable isotope ratio mass spectrometer. Results show a decrease in the oxygen isotope fractionation factor ($\alpha^{18}O$) by 2.4 ‰ with increasing growth rate of aragonite spherulites from 0.064 to 0.88

nm/s (5.5-76 μm/day). Crystal growth rate is therefore potentially an important consideration when using $\delta^{18}O$ in natural carbonates as a proxy for ocean and terrestrial climate. Growth Entrapment Model (GEM) was applied to explain experimentally determined $\alpha^{18}O$-V relationships, assuming lattice-fluid equilibrium $\alpha^{18}O$ values (0% of growth entrapment) at slow growth rates and complete disequilibrium fractionation (100% of growth entrapment) during fast crystallization. Although V values obtained experimentally do not fully cover the V range used in GEM, the combination of experiment and simulations suggest depletion of ^{18}O in the near-surface region of aragonite relative to the bulk crystal lattice. This ^{18}O-depleted zone can be "captured" during rapid (non-equilibrium) crystal growth.

Keywords:
Aragonite
Oxygen isotopes
Isotopic fractionation factor
Growth rate
SIMS
Disequilibrium

Introduction

The oxygen isotope composition in biogenic and abiogenic calcium carbonate minerals was proven to be a powerful tool in paleoclimatology (Urey 1947; Epstein et al. 1953; Broecker 1986; Labeyrie et al. 1987; Lea et al. 2000; etc.). However, there are certain complications in $\delta^{18}O$-based temperature reconstruction. Among them is the presence of isotopic heterogeneity up to 5 ‰ in deep sea corals presumably grown at near-constant environmental conditions (Adkins et al. 2003; Rollion-Bard et al. 2010). In addition, calculated and observed $10^3 \cdot \ln\alpha^{18}O$-temperature relationships provide inconsistency of up to 3 ‰, which results in the temperature offsets as large as 13°C (Grossman and Ku 1986; Patterson et al. 1993; Thorrold et al. 1997; Zheng 1999; Boehm et al. 2000; Kim et al. 2007). Furthermore, kinetic isotopic fractionation

was observed between inorganically precipitated aragonites and fluid at 25°C (Zhou and Zheng 2003; Kim et al. 2006). Zhou and Zheng (2003) observed $10^3 \cdot \ln\alpha^{18}O$ vary from 27.35 to 28.51 ‰. Additionally, $10^3 \cdot \ln\alpha^{18}O$ decreases from 29.2 to 28.8 ‰ with increasing of aragonite precipitation rate at constant pH of 8.2 (Kim et al. 2006).

Growth entrapment model (GEM) was applied to experimental data. GEM developed by Watson and co-workers (Watson and Liang 1995; Watson 1996; Watson 2004) was successfully applied for quantitative description of experimental data on element partitioning and isotopic fractionation from the works of Lorens (1981), Tesoriero and Pankow (1996), Stoll et al. (2002), Tang et al. (2008 a,b), and Gabitov et al. (2008). GEM describes disequilibrium fractionation of elements and isotopes between a crystal and its growth medium as a consequence of the "capture" of a chemically and isotopically anomalous near-surface region of the lattice during crystal growth. In this model, the extent of fractionation is determined in part by the parameter F, which is the *equilibrium* partition coefficient (or fractionation factor) between the near-surface and the deeper lattice (whose value is unknown *a priori*). X-ray reflectivity and computer simulation data showed this few angstroms thick near-surface region of calcite is structurally relaxed relative to the normal lattice (Fenter et al. 2000; Rohl et al. 2003). Another consideration in GEM is solid state diffusion in the near-surface region of calcite (D_s) is much faster than in the crystal lattice (D_l) in analog with diffusion along the surfaces of grain boundaries. Indeed, the work of Stipp et al. (1992) suggested that D_s of Cd in calcite is many orders of magnitude faster than D_l. Watson and co-workers consider that composition of growing crystal depends on V and D_s: a 100% entrapment of the surface composition at high V, when D_s is ineffective; an equilibrium fractionation (0% entrapment) when D_s dominates over V. At intermediate growth rates, partial

growth entrapment happens. *Ab initio* molecular dynamics simulations of Ti^{4+} in the near-surface region of quartz confirmed the validity of GEM (Lanzillo et al., in review). They quantitatively demonstrated that Ti^{4+} vacancy-formation energy in the outermost monolayers of α quartz is significantly smaller that in the bulk lattice. The fast Ti diffusivity in the near surface region of quartz was confirmed by additional findings of their work where the activation energy for Ti diffusion decreases steeply toward the crystal surface in the 2-3 outermost monolayers. GEM is not the only possible explanation for non-equilibrium uptake of isotopes. DePaolo (2011) attributes the phenomenon entirely to surface reaction kinetics that depend on isotope identity. Contrary to GEM, this model considers reaction in the liquid layer at the calcite/fluid interface. The key parameters in DePaolo (2011) model are net precipitation rate *Rp* and backward reaction rate *Rb*. The equilibrium isotopic fractionation is approached when $Rp/Rb<<1$. This criterion is somewhat similar to growth Péclet number ($Pe=V\cdot l/D_S$) used in GEM, where *l* is half-thickness of the enriched surface layer of the crystal. Both models can explain the disequilibrium element partitioning and isotopic fractionation data of Lorens (1981), Tesoriero and Pankow (1996), Gabitov and Watson (2006), and Tang et al. (2008a,b) through kinetics of ion attachment to the mineral surface (DePaolo 2011; Nielsen et al. 2012) and through growth entrapment (Watson 2004). However, the DePaolo model does not consider the well-established fact that the atomic structure of calcite and other minerals differs from that of the bulk lattice to distances of ~1 nm from the surface (e.g., Fenter 2000).

Experimental and analytical methods

Aragonite precipitation

Experiments were performed in the Department of Earth and Space Sciences at UCLA. The aragonite growth method was adapted from previous studies (Gruzensky 1967; Paquette and Reeder 1995) and modified by addition of Mg into fluid and introduction of sub-sampling and multiple REE spikes (Gabitov et al. 2008 and 2012). Crystals grew by diffusion of CO_2 into Ca-bearing fluid at room temperature of 24.2±0.8°C. Pyrex beaker was filled with 1 liter of solution and placed into 0.3x0.3x1 m^3 closed plastic box where air was enriched in CO_2 by decomposition of ammonium carbonate. Petri dish with diameter of 15 cm was placed into a box to increase humidity and decrease the evaporation of experimental fluid. Temperature of solution was measured four times per day and no correlation between day and night were observed. The aragonite crystallization was promoted by elevation of Mg/Ca in fluid (similar to Mg/Ca in seawater), which suppressed calcite nucleation (Berner 1966; De Groot and Duyvis 1966; Möller and Parekh 1975; Mucci and Morse 1983; Davis et al. 2000). The initial solution was prepared by dissolving NH_4Cl in deionized (DI) H_2O to the concentration of 0.5 mol/l, along with minor amounts of reagent grade $CaCl_2 \cdot 2H_2O$ (0.01), $MgCl_2 \cdot 6H_2O$ (0.05), $SrCl_2 \cdot 6H_2O$ (10^{-4}), $BaCl_2 \cdot 2H_2O$ ($4 \cdot 10^{-7}$), $LiOH \cdot H_2O$ ($5 \cdot 10^{-4}$), H_3BO_3 ($5 \cdot 10^{-3}$), and U ICP-MS standard ($2 \cdot 10^{-7}$) [values in parentheses are concentrations in mol/l]. The pH of the solution was adjusted to 5.94 by addition of reagent grade NaOH. Aragonite precipitated as needle-like crystals with a thickness of a few microns, radiating from a central point to form bundles of generally hemispherical shape. Hereafter these bundles are referred to as spherulites. Aragonite continuously nucleated at the surface of the solution and on the inner walls of the container. The onset of nucleation was not determined directly, but was estimated from the time interval between two visual observations as 13 hours prior to addition of Sm. The fluid was not stirred during aragonite precipitation; however, the solutions were mixed after addition of each REE

spike by repeated injection and withdrawal of fluid using a 60-ml syringe. REE spikes (Sm, La, Nd, and Tb) were sequentially introduced into the growth medium in the amount of 1 ml of diluted REE-bearing solution, which yielded an estimated REE concentration range in the solution from 10 to 50 ppb. Rare-earth elements are compatible in aragonite (Akagi et al. 2004; Wyndham et al. 2004); thus their injection into the growth solutions provided a useful time markers in the crystals. The first REE spike (Sm) was introduced into solution as soon as the first aragonites became visible with the naked eye. The fluids were sampled periodically for measurement of pH, and stored in a refrigerator for future use. The pH (NBS-scale) was measured immediately after collection of the fluid using an OAKTON pH 510 meter with "All-in-One" pH/Temp electrode calibrated with 7.00 and 10.00 pH (Fig. 1a). pH drifted from 8.27±0.09 to 8.62±0.02 during aragonite precipitation (Fig. 1b and Table 1). At the end of the run, aragonite spherulites were recovered with a spatula and quickly rinsed with DI H_2O and methanol.

Synthetic fluids and aragonite were analyzed for $\delta^{18}O$ with Finnigan gas-source (GS) isotope ratio mass spectrometers Delta S and MAT 252 respectively in the Environmental Isotope Laboratory at the University of Arizona. Precision was 0.08 ‰ on the basis of repeated internal standards.

In situ analyses of aragonite

Sample preparation

The largest aragonite spherulites were mounted in epoxy (EpoxiCure®, Buehler) such that the flat side of the hemi-spherulite was exposed for SIMS analysis. The mounts were polished and the crystals were examined with CAMECA ims 1270 ion microprobe at UCLA, first for oxygen isotopes (analytical sessions 1and 2) and subsequently for Ca and REE (session-3).

Reflected and transmitted light microscopy images of the polish section are shown on the Figure 2. Here reflected light image contained burn marks where $\delta^{18}O$ data have been collected in the edges and the center of the aragonite spherulite (Figure 2a). Transmitted light image shows spherulites are formed by aragonite needles growing radial from the centers on nucleation (Figure 2b). This observation is consistent with those of Holcomb et al. (2009), where two types of morphology were observed in synthetic aragonites: sub-micron size granular aragonite in the center and blade-like fibrous crystals growing outward.

$\delta^{18}O$ analyses by SIMS

Aragonite spherulites were examined with a 0.2 nA primary beam with a lateral dimension of 10-15 µm at the sample surface (session 1). Negative secondary ions ^{16}O and ^{18}O were simultaneously measured by Faraday Cup (FC, C) and electron multiplier (EM, H2) using multi-collection set-up for a mass resolving power (MRP) of ~2000, which is sufficient for resolving hydride interference with the ^{18}O peak (Fayek et al. 2002). FC background and EM dead time corrections were performed for each measurement. Raw intensity of the minor isotope varied from $1.4 \cdot 10^5$ to $1.6 \cdot 10^5$ counts per second (cps). An additional analytical session (no. 2) was devoted to the same spherulites using 3-5 nA Cs^+ primary beam with a lateral dimension of 20-30 µm at the sample surface (see Gabitov et al. 2012 for more details). ^{16}O and ^{18}O were measured simultaneously by Faraday Cups (FC) using multi-collection detectors L'2 and H'2. No isotopic fractionation was observed by rotating sample mount by 90°. The raw intensity of the minor isotope varied from $7 \cdot 10^6$ to 10^7 cps. The total sputtering time prior to acquisition was 120 s, which was sufficient to reach a steady $^{18}O/^{16}O$ value over the 12 cycles of the analysis on a single spot in both analytical sessions. 10 spot analyses of calcium carbonate reference materials (calcites and aragonite) yielded standard deviation of 0.2-0.3 ‰.

Standard was analyzed routinely after every 5-8 measurements of the aragonite sample. In order to quantify SIMS data intensity ratios of $^{18}O/^{16}O$ were standardized internally to the reference $^{18}O/^{16}O$ obtained from the bulk GS isotopic analyses (see Appendix-1 for details).

Aragonite spherulites were characterized with SIMS spot profiles (traverses) from one edge to another. Imaging with an interference microscope (PHASE SHIFT MicroXAM Surface Mapping Microscope Crystal) revealed slight relief on the sample surfaces in the sense that the spherulite edge was elevated 0.2-03 µm above the spherulite center. The same relief was noted on the standard grains of similar size and no correlation in $\delta^{18}O$ with the distance from the edges of standard grains was observed. Therefore, measured $\delta^{18}O$ was not affected by sub-micron grain relief. The depths of the craters produced by Cs^+ beam were 1.5 and 4 µm in both sample and standard materials at primary beam intensities used in the analytical sessions 1 (0.2 nA) and 2 (3-5 nA) respectively. In between the first and second analytical sessions, a thin layer of aragonite (2 µm thick) was removed by fine polishing. Because of the re-polishing, a small shift in x-y coordinates is possible, but this is insignificant relative to the volume of sputtered aragonite (>75 μm^3 in session-1 and >800 μm^3 in session-2).

Ca and REE analyses by SIMS

Following $\delta^{18}O$ determinations, REE and Ca analyses (session-3) were performed on the top of the burn marks from $\delta^{18}O$ measurements. Calcium and REE were measured with a 1-12 nA $^{16}O^-$ primary beam at 20-30 µm lateral dimension on the sample surface with a voltage offset of -60 V using the energy bandwidth of 50 V (see Gabitov et al. 2012 for details). Positive secondary ions corresponding to mass/charge stations of 41.7 (background), ^{42}Ca, ^{88}Sr, ^{139}La, ^{143}Nd, ^{149}Sm, and ^{159}Tb were measured in mono collection mode with electronic multiplier.

Rare-earth analyses revealed regions of the crystals representative of specific aragonite growth intervals, and thus allowed reconstruction of the evolution of growth over time.

Results

Precipitated phase was identified as aragonite because of crystal morphology and measured Sr/Ca, which corresponds to those calculated from $(Sr/Ca)_{fluid}$ and partition coefficient between aragonite and fluid (Kinsman and Holland 1969; Gaetani and Cohen 2006). Furthermore, aragonite was the only phase detected by X-ray diffraction analysis in the analogous experiment (Gabitov et al. 2008).

Isotopic composition of fluids and aragonite via bulk analyses

Isotopic analyses of aragonite yielded $\delta^{18}O_{VPDB}$ of -13.49 ‰. The composition of the fluid ($\delta^{18}O_{SMOW}$) increased during the experiment by 2.24 ‰ (see Table 1 and Discussion). However, initial $\delta^{18}O_{SMOW}$ of -10.63 ‰ did not correspond to the onset of aragonite crystallization, which started sometime before addition of Sm spike. Therefore, $\delta^{18}O_{SMOW}$ fell between -10.63 and -9.07 ‰ at the onset of aragonite nucleation.

In situ determined growth rates and fractionation factors

Oxygen isotope fractionation factors were determined for each SIMS analytical spot and are presented in the Table 2. Values of $\alpha^{18}O$ were determined at 23 spots as profiles through aragonite spherulites. The whole range of measured $10^3 \cdot \ln(\alpha^{18}O)$ is from 24.37 to 28.49 ‰ (Table 2). The values of $\alpha^{18}O$ always decreased from the edges to the centers of individual spherulites. SIMS analyses of REE demonstrated that spherulites recorded the REE signals corresponding to the introduction of REE into growth medium. Growth rates were determined as the length of each zone (Δx) in each analytical profile divided by the time between REE spikes (Δt) (Appendix-2, Figure S-1). Here, the ion beam burn marks from the $\delta^{18}O$ analyses

are shown on the reflected light image. The Sm and La arrows show the locations where REE were detected. The distance between Sm and La corresponds to the aragonite layer grown between their addition into fluid, which $\delta^{18}O_w$ was calculated as an average between solutions collected immediately after additions of Sm and La. Growth rates from "prior Sm" zones were estimated from the time between the absence of crystallization and when crystals became observable in the flask (addition of Sm spike).

Oxygen isotope fractionation factors ($\alpha^{18}O$) were calculated for each spiked growth layer of aragonite as $\alpha^{18}O = [^{18}O/^{16}O(t)_{aragonite}]/[^{18}O/^{16}O(t)_{fluid}]$, where $^{18}O/^{16}O(t)_{aragonite}$ is the data from multiple or individual SIMS spots collected in particular REE-spiked zone of the aragonite and $^{18}O/^{16}O(t)_{fluid}$ is the corresponding fluid isotopic value (Table 3). Uncertainties of $10^3\ln(\alpha^{18}O)$ are expressed as the standard error (s.e.) of the multiple measurements (n) or as s.e. of the 12 analytical cycles of the individual spot measurements (n=1) (Figure 3a). The value $10^3\ln(\alpha^{18}O)$ decreases by 3.26 ‰ (from 28.35 to 25.09 ‰) with increasing aragonite growth rate from 0.026 to 1.17 nm/s (Figure 3a). Here, only two data were based on multiple SIMS analyses with the number (n) shown on the plot. Remained data were obtained from individual SIMS measurements (n=1) where thickness of the aragonite zone precipitated between addition of REE spikes was small and similar to the size of the ion beam. The errors of V determined from the size of the ion beam divided by the time between REE spiking were large and similar to the absolute value of V. In order to estimate statistically significant growth rate uncertainties the mean V and $10^3\ln(\alpha^{18}O)$ values were calculated by averaging the adjacent data with n=1 (Figure 3b). The groups of averaged data are marked by contours in Figure 3a. The datum where V=0.1710 nm/s and $10^3\ln(\alpha^{18}O)$=27.53 ‰ (n=5) was left unchanged (Figure

3b). Averaged $10^3\ln(\alpha^{18}O)$ decrease from 28.14 to 25.65 ‰ with increasing of growth rate from 0.0641 to 00.8788 nm/s (Table 3, Figure 3b)

Discussion

The increase of $\delta^{18}O_{fluid}$ by 2.24 ‰ is likely due to evaporation of 0.09 volume fraction of the fluid (determined by volume change) during experiment. This result is consistent with water evaporation experiment in air of Luz et al. (2009). However, evaporation could not cause the increase of $\alpha^{18}O$ with time (i.e. from center toward the edges of shperulite), because drift in $\delta^{18}O_{fluid}$ was considered in the calculation of $\alpha^{18}O$.

With increasing growth rate $10^3\alpha^{18}O$ decreases toward $10^3\alpha^{18}O_{eq}(CO_3^{2-}$-fluid) (Table 3, Fig. 4). This implies that CO_3^{2-} is the major source of ^{18}O in aragonite, which is consistent with modeling and *in situ* characterization of the calcite/H_2O interface (van Cappellen et al. 1993; Stipp 1999; Fenter et al. 2000). The change of pH in our experiment cannot explain the observed $\alpha^{18}O$-V trend during aragonite precipitation (Table 1). The pH in our fluid increased from 8.27±0.09 to 8.62±0.02 during crystallization, but $\alpha^{18}O$ increases, in opposition to the trend expected from the studies of Usdowski and Hoefs (1993) and Zeebe (1999, 2007). They suggested that increasing pH causes enrichment of CO_3^{2-} in the fluid, which decreases the value of $\alpha^{18}O$. My data cannot be explained by this mechanism. The present study confirms the directions of the $10^3\cdot\ln\alpha^{18}O$ - precipitation rate trend observed in the study of Kim et al. (2006), and found a much stronger effect of growth rate on $10^3\cdot\ln\alpha^{18}O$. Data from present work are relevant to natural materials, because the range of growth rates overlaps with extension rates of corals and speleothems (Harriott 1998; Watanabe et al. 2003; Brahmi et al. 2010; Li et al. 2011). *In situ* determined growth rates of scleractinian coral using calcein labeling are

consistent with the slowest rates of synthetic aragonites from present work (Brahmi et al. 2010; Gagnon et al. 2012).

The growth entrapment model (GEM) of Watson and co-workers was used to test the experimental data (see Appendix-3). The range of growth rates obtained experimentally ($0.05<V<0.88$ nm/s) is smaller than V range used in GEM simulations ($10^{-4}<V<30$ nm/s) (Figure 4). However, the combination of experimental and simulating results suggest the near surface region of aragonite is depleted in ^{18}O relative to the lattice at equilibrium, i.e. surface enrichment factor F is less than unity and equal to 0.994605. Obtained $\alpha^{18}O$ are consistent with GEM simulations, which implies fast diffusivity of oxygen (0.2 nm^2/s) in the near-surface layer of aragonite. Two different values of D_s used in previous works (0.01 and 0.06 nm^2/s) were applied in simulations for comparison. GEM simulations results suggest equilibrium fractionation occurs at the growth rates slower than 0.01 nm/s, where no growth entrapment occurs. The 100% entrapment happens at high growth rates (V>10 nm/s), where $10^3 \cdot \ln\alpha^{18}O = 10^3 \ln\alpha^{18}O(CO_3^{2-}\text{-fluid}) = 23.71$ ‰, which is ~5 ‰ lower than suggested equilibrium $10^3 \ln\alpha^{18}O = 29.12$ ‰ (Kim et al. 2006). Therefore, extreme growth rates (V<0.01 and V>10 nm/s) result in an apparent temperature offset of ~23°C, confirming growth rate effects should be considered in evaluation of oxygen isotope temperatures derived from naturally occurring aragonite. The $10^3 \ln\alpha^{18}O$ data range of slowly grown corallite sponges (0.0047-0.12 nm/s) overlaps with those from slow growth experiment of Kim et al. (2006) at 25°C and GEM data, i.e. 29.08-29.34 ‰ compared to 29.12 ‰ (Böhm et al. 2000; Rosenheim et al. 2009). Contrary, high $10^3 \ln\alpha^{18}O$ values (29.71-29.88) in fast grown fish otoliths (2.3-5.8 nm/s) were published by Thorrold et al. (1997) and do not confirm GEM and experimental data, indicating the potential of biologically controlled aragonite growth. This direct comparison of growth rates is

an approximation due to biologically induced episodic growth of bio-aragonite. Terrestrial inorganically precipitated carbonate deposits show partial consistency with experimental data as well as marine samples. Data from very slowly precipitated cave calcite ($V<10^{-4}$ nm/s) support the enrichment of ^{18}O in calcite ($10^3 ln\alpha^{18}O$ =29.80) grown at conditions close to equilibrium (Coplen 2007; Dietzel et al. 2009; Gabitov et al. 2012). However, the high $10^3 ln\alpha^{18}O$ (29.91) of rapidly precipitated travertines at 24.2°C reported by Deák et al. (2011) are not consistent with experimentally derived $\alpha^{18}O$-V relationship of present study. Therefore, the effect of depositional rate on oxygen isotopic composition of travertines should be examined separately. A more complex precipitation might be due to pressure release at the vents or capture of isotopically non-equilibrated CO_3^{2-} at growth rates much faster than achieved experimentally.

In order to compare $\alpha^{18}O_{aragonite}$-V with $\alpha^{18}O_{calcite}$-V all of these data are combined in Figure 4. GEM simulations are shown for aragonite data only. Calcite data complement the slow growth rate region on this plot. Here, aragonite and simulating data at D_s=0.2 nm^2/s are in between $10^3 \cdot ln\alpha^{18}O_{calcite}$-V trends evaluated by Dietzel et al. (2009) and Gabitov et al. (2012). The D_s value 0.06 nm^2/s previously reported by Tang et al. (2008a,b) partially fits the data of Dietzel et al. (2009). The growth rates in Gabitov et al. (2012) were evaluated *in situ* from REE spikes as well but with larger dataset due to a large size of calcite crystals. The growth rates in nm/s for the data of Dietzel et al. (2009) were calculated from their reported bulk precipitation rates (μmol/m^2/s) using the molar volume of calcite (36.99 cm^3/mol). This conversion assumes growth of a single crystal, not a collection of small crystals (up to 5 μm in size) such as those described by Dietzel et al. (2009). Their recalculated V could be underestimated for this reason. The absence of the error bars in their data on bulk precipitates corresponds to the

unresolved intra-crystalline variability with gas-source mass spectrometry. The observed difference in ^{18}O fractionation between calcite and aragonite does not support the previously reported analytical and calculated data on biogenic and inorganically grown $CaCO_3$ where $\alpha^{18}O_{calcite\text{-}fluid}$ is lower than $\alpha^{18}O_{aragonite\text{-}fluid}$ by 0.4-1.4 ‰ (Tarutani et al. 1969; O'Neil et al., 1969; Grossman and Ku 1986; Patterson et al. 1993; Kim and O'Neil, 1997; Thorrold et al. 1997; White el al. 1999; and Böhm et al. 2000; Kim et al., 2007). Obtained data are more relevant to calculations of Zheng (1999) and natural observations of Epstein et al. (1953), Behrens and Land (1972), and Horibe and Oba (1972) showing ^{18}O enrichment in calcite relative to aragonite by ~1.5 ‰ when $0.06<V<0.3$ nm/s (this study and Gabitov et al. 2012). The presence of smaller correlation of $10^3 \cdot \ln\alpha^{18}O$ with V in calcite relative to aragonite is likely because the study of Gabitov et al. (2012) did not capture the full range of possible $\alpha^{18}O_{calcite}$ values, from complete equilibrium to 100% growth entrapment. The assumed equilibrium value of $\alpha^{18}O_{aragonite}$ (Kim et al. 2006) used in the simulations overlaps with the $\alpha^{18}O_{calcite}$ for slowest grown calcites from the experiments of both Dietzel et al. (2009) and Gabitov et al. (2012) within standard error at 1σ level. For this reason, the present results probably cannot be used for evaluating difference between equilibrium values of $\alpha^{18}O_{aragonite}$ and $\alpha^{18}O_{calcite}$. However, growth rate dependence of $\alpha^{18}O_{aragonite}$ was clearly demonstrated in this study, and the new data provide the first evidence from *in situ* analyses that high growth rate of individual spherulites causes depletion of ^{18}O in the aragonite lattice and $\alpha^{18}O$ approaches the value of $\alpha^{18}O_{eq}(CO_3^{2-}\text{-fluid})$.

Acknowledgments. I would like to thank Axel Schmitt, Kevin McKeegan, and Mark Harrison for their help and support with the experiments and ion microprobe measurements. I am grateful to Bruce Watson for inspiring me, providing GEM code, and discussing the results of this work. I also thank David Dettman for fluid $\delta^{18}O$ analyses. I would like to acknowledge the Editor-in-Chief Uwe Brand, Ethan Grossman, and an anonymous reviewer for their comments

on the manuscript; Dina Gabitov for her help with manuscript preparation; Johanna Marin-Carbonne for sharing SIMS operation time. Experiments and SIMS analyses were supported by U.S. NSF, EAR, Instrumentation and Facilities Program. GS mass spectrometry analyses were covered by UC MEXUS grant 443875-MH-19931-03.

Appendix-1. SIMS IMF for standards and sample

Natural clear-beige aragonite crystal (BB-Ar) from Belice, Bohemia and calcites (NBS-18, NBS-19, and MEX) were analyzed to determine SIMS instrumental mass fractionation [$IMF=10^3\cdot\ln(^{18}O/^{16}O_{SIMS})/(\ ^{18}O/^{16}O_{reference})$]. IMF values for calcite standards ($IMF_{calcite}$) were consistent to each other within analytical uncertainty, but lower than IMF of aragonite (IMF_{BB-Ar}), i.e. IMF_{BB-Ar}-$IMF_{calcite}$=2.1 and 0.8 ‰ in the analytical sessions 1 and 2 respectively. IMF of synthetic aragonite sample (IMF_{sample}) was significantly lower than those for aragonite standard, i.e. IMF_{BB-Ar}-IMF_{sample}=6 and 4 ‰ in the sessions 1 and 2 respectively. The reason for this phenomenon is probably the polycrystalline nature of aragonite spherulites, which yields the different ionization efficiency relative to monocrystalline standards. Therefore, internal standardization was applied for quantifying SIMS data, i.e. the data from the single SIMS spots were normalized to the mean value of all SIMS data collected in the particular spherulite and multiplied to the sample $^{18}O/^{16}O$ obtained with GS mass spectrometry.

Appendix-2. Evaluation of aragonite growth rate

The example of transmitted light microscopy image shows locations of three SIMS $\delta^{18}O$ analyses collected in the center and at the edges of aragonite spherulite (Figure S-1-A). The locations of those spots were determined from the beam burn marks in the reflected light image of the same spherulite (Figure S-1 B). Locations of REE spot analyses are presented as well. The evaluation of growth rate is illustrated as the schematic on the (Figure S-1-C). Here the observed REE pattern yielded only one V value that corresponds to the $\delta^{18}O$ analytical spot collected at the left edge of spherulite. The appearance of REE corresponds to the sequence of its addition into fluid; i.e., starting with Sm and following by La in this example. REE spot-1 (dashed oval marker) contains the highest REE/^{42}Ca ratios. Spot-2 has similar ^{149}Sm/^{42}Ca, but lower ^{139}La/^{42}Ca, ^{143}Nd/^{42}Ca, and ^{159}Tb/^{42}Ca than REE spot-1 by the factors of 2.6, 47, and 65 respectively. Therefore, spot-2 grew after addition of Sm into fluid. However, La was introduced during the growth of aragonite layer covered by spot-2, i.e. the thickness of La contained layer is 1:2.6 of the spot-2 size (Figure S-1-C). Here the growth rate is equal to the ratio of the distance Δx and time interval between addition of Sm and La. The REE/^{42}Ca data are presented in the supplemental Table (S-1).

Appendix 3. Parameters for the growth entrapment model

The simulations were conducted with the new version of the GEM code (GEM2) running with Quick Basic program (QB64). The description of the model is presented by Watson (2004), where he considered concentration of ^{18}O changes as the function of the distance from the surface of the crystal:

$$^{18}O(x)=^{18}O_{eq}\cdot F^{\exp(x/l)} \qquad \text{(A1.1)}$$

where $^{18}O(x)$ is the concentration of ^{18}O in the crystal at some distance x from the surface, $^{18}O_{eq}$ is the concentration reflecting fractionation equilibrium between the growth medium and the bulk crystal, F is the surface enrichment factor and l (0.5 nm) is the half-thickness of the enriched surface layer. The value of F was set to 0.994605, which is the ratio of $\alpha_{eq}(CO_3^{2-}$-fluid)=1.023993 to α_{eq}(aragonite-fluid)=1.029548, reported in Kim et al. (2006). Mg/Ca of the fluid in their work was set to 4 mol/mol in comparison to our initial fluid value Mg/Ca 5 mol/mol.

The diffusivity of oxygen in the aragonite lattice (D_l) was extrapolated from the high temperature calcite data of Farver (1994) as ~$3.4 \cdot 10^{-21}$ nm^2/s. The diffusion in lattice is very slow and can not compete with those in the near surface layer of aragonite. Changing the lattice diffusion coefficient (D_l) by an order of magnitude does not visually affect the GEM fit and will not reasonably affect the resulting F and D_s values taking into account uncertainties in V and $1000\ln(\alpha^{18}O)$. The parameters of D_s and distance multiplier (m) were optimized for obtaining the best fit of $10^3 \cdot \ln\alpha^{18}O$ experimental data, i.e. D_s=0.2 nm^2/s and m=∞. The meaning of infinite m is the diffusivity is independent of depth in the crystal (and equal to D_s) over a distance much greater than the thickness of the compositionally distinct near-surface layer. For comparison of GEM parameters that were used in this study and other works please see Table A-2. The range of obtained D_s values unlikely could be used to evaluate diffusivity difference between O, Ca, Mg, and Sr in aragonite and calcite. It's probably related to experimental designs, i.e. how the growth rates were evaluated.

Table A-2. Parameters used in GEM calculations for the data from this study and other works at 22 and 25°C.

element or isotope	phase	K_{eq} or α_{eq}	F	D_l (nm^2/s)	D_s (nm^2/s)	l (nm)	m	growth rate determination	Reference
^{18}O*	aragonite	1.029548	0.994605	~10^{-21}	0.2	0.5	∞	spikes (nm/s)	This work
Mg	aragonite	$1.9 \cdot 10^{-5}$	53	0	0.01	0.5	∞	spikes (nm/s)	Gabitov et al. (2008)
^{44}Ca	calcite	1	0.99825	~10^{-18}	0.06	0.5	8	mean surf. area (µmol/m^2/h)	Tang et al. (2008a)
Sr	calcite	0.02	12.5	~10^{-18}	0.06	0.5	8	mean surf. area (µmol/m^2/h)	Tang et al. (2008b)
Sr $^{\#}$	calcite	0.02	10	~10^{-18}	0.01	0.5		const. surf. area (nmol/mg/min)	Stoll et al. (2002)

(*) - α_{eq}(aragonite-fluid) and $\alpha_{eq}(CO_3^{2-}$-fluid) from Kim et al. (2006)
($^{\#}$) - Fitting experimental data of Lorens (1981) and Tesoriero and Pankow (1996)
spikes = addition of REE spikes to evaluate mineral growth rates;
mean surf. area = mean specific surface area was used in calculation of precipitation rates due to the significant change of the surface area during calcite growth;
const. surf. area = specific surface area does not change significantly during calcite growth.

References

Adkins J.F., Boyle E. A., Curry W. B. and Lutringer A. (2003) Stable isotopes in deep-sea corals and a new mechanism for "vital effects". *Geochim. Cosmochim. Acta*, **67**, 1129–1143.

Akagi T., Hashimoto Y., Fu F-F..; Tsuno H., Tao H., and Nakano Y. (2004) Variation of the distribution coefficients of rare earth elements in modern coral-lattices: species and site dependencies. *Geochim. Cosmochim. Acta*, **68**, 2265-2273.

Berner N.A. (1966) Diagenesis of carbonate sediments: interaction of magnesium in sea water with mineral grains. *Science*, **153**, 188-91.

Behrens E. W. and Land L. S. (1972) Subtidal Holocene dolomite, Baffin Bay, Texas. *J. Sed. Petrol.*, **42,** 155–161.

Böhm F., Joachimski M. M., Dullo W.C., Eisenhauer A., Lehnert H., Reitner J., and Wörheide G. (2000) Oxygen isotope fractionation in marine aragonite of coralline sponges. *Geochim. Cosmochim. Acta*, **64**, 1695–1703.

Brahmi C. , Meibom A., Smith D. C., Stolarski J., Auzoux-Bordenave S., Nouet J., Doumenc D., Djediat C., and Domart-Coulon I. (2010) Skeletal growth, ultrastructure and composition of the azooxanthellate scleractinian coral Balanophyllia regia. *Coral Reefs*, **29**, 175–189, DOI 10.1007/s00338-009-0557-x

Broecker W. S. (1986) Oxygen isotope constraints on surface ocean temperatures. *Quat. Res.* **26,** 121-134.

Davis K.J., Dove, P.M., and De Yoreo J.J. (2000) The role of Mg^{2+} as an impurity in calcite growth. *Science*, **290**, 1134-1137.

De Groot K. and Duyvis E.M. (1966) Crystal form of precipitated calcium carbonate as influenced by adsorbed magnesium ions. *Nature*, **212**, 183 – 184.

Deák J., Kele S., Fórizs I., Demény A., and Scheuer G. (2011) Calculation of temperature and $\delta^{18}O$ of depositing water by measured $\delta^{18}O$ of recent travertines deposited from the Budapest thermal karst water. *Cent. Eur. Geol.* **54**, 157–165.

DePaolo D.J. (2011) Surface kinetic model for isotopic and trace element fractionation during precipitation of calcite from aqueous solutions Source. *Geochim. Cosmochim. Acta*, **75**, 1039-1056.

Dietzel M., Tang J. W., Leis A., and Kohler S. J. (2009) Oxygen isotopic fractionation during inorganic calcite precipitation - Effects of temperature, precipitation rate and pH. *Chem. Geol.*, **268**, 107-115.

Epstein S., Buchsbaum R., Lowenstam H. A., and Urey H. C. (1953) Revised carbonate-water isotopic temperature scale. *Geol. Soc. Am. Bull.* **64,** 1315–1325.

Farver J. R. (1994) Oxygen self-diffusion in calcite: Dependence on temperature and water fugacity. *Earth Planet. Sci. Lett.* **121,** 575–587.

Fayek M., Harrison T. M., Ewing R. C., Grove M., and Coath C. D. (2002) O and Pb isotopic analyses of uranium minerals by ion microprobe and U-Pb ages from the Cigar Lake Deposit. *Chem. Geol.* **185,** 205–225.

Fenter P., Geissbuhler P., Dimasi E., Srajer J., Sorensen L.B., and Sturchio N.C. (2000) Surface speciation of calcite observed in situ by high-resolution X-ray reflectivity**.** *Geochim. Cosmochim. Acta*, **64**, 1221-1228.

Friedman I., O'Neil J., and Cebula G. (1982) Two New Carbonate Stable-Isotope Standards. *Geostand. Newslett.*, **6**, 11-12.

Gabitov R. I., Gaetani G. A., Watson E. B., Cohen A. L. and Ehrlich H. L. (2008) Experimental determination of temperature and growth rate effects on U^{6+} and Mg^{2+} partitioning between aragonite and fluid. *Geochim. Cosmochim. Acta*, **72**, 4058–4068.

Gabitov R.I., Watson E.B., and Sadekov A. (2012) Oxygen isotope fractionation between calcite and fluid as a function of growth rate and temperature: An in situ study. *Chem. Geol.* **306-307**, 92-102.

Gaetani G.A. and Cohen A.L. (2006) Element partitioning during precipitation of aragonite from seawater: A framework for understanding paleoproxies. *Geochim. Cosmochim. Acta* **70**, 4617-4634.

Gagnon A.C., Adkins J.F., and Erez J. (2012) Seawater transport during coral biomineralization. *Earth Planet. Sci. Lett.*, **329-330**, 150–161.

Grossman E. L. and Ku T. L. (1986) Oxygen and carbon isotope fractionation in biogenic aragonite. Temperature effects. *Chem.Geol.* **59,** 59–74.

Gruzensky P.M. (1967) Growth of calcite crystals. *J. Phys. Chem. Solids*, S **1**, 365-367.

Harriott V. J. (1998) Growth of the staghorn coral *Acropora Formosa* at Houtman Abrolhos, Western Australia. *Mar. Biol.*, **132**, 319-325.

Horibe Y. and Oba T. (1972) Temperature scales of aragonite-water and calcite-water systems. *Fossils* **23/24,** 69–79.

Kim S-T. and O'Neil J.R. (1997) Equilibrium and nonequilibrium oxygen isotope effects in synthetic carbonates. *Geochim. Cosmochim. Acta* **61**, 3461–3475.

Kim S.-T., Hillaire-Marcel C. and Mucci A. (2006) Mechanisms of equilibrium and kinetic oxygen isotope effects in synthetic aragonite at 25°C. *Geochim. Cosmochim. Acta*, **70**, 5790-5801.

Kim S.T., O'Neil J.R., Hillaire-Marcel C., and Mucci A. (2007) Oxygen isotope fractionation between synthetic aragonite and water: Influence of temperature and Mg^{2+} concentration *Geochim. Cosmochim. Acta*, **71**, 4704-4715.

Kinsman D.J.J. and Holland H.D. (1969) The co-precipitation of cations with $CaCO_3$-IV. The co-precipitation of Sr^{2+} with aragonite between 16 and 96°C. *Geochim. Cosmochim. Acta* **33**, 1-17.

Labeyrie L. D., Duplessy J.-C., and Blanc P. L. (1987) Variations in mode of formation and temperature of oceanic deep waters over the past 125,000 years. *Nature* **327,** 477-482.

Lanzillo N.A., Watson E.B., Thomas J.B., Nayak S.K., and Curioni A. Near-surface controls on the composition of growing crystals: MD simulations of Ti^{4+} energetics and diffusion in alpha quartz. *In review.*

Lea D.W., Pak D.K., and Spero H.J. (2000) Climate Impact of Late Quaternary Equatorial Pacific Sea Surface Temperature Variations. *Science*, **289**, 1719-1724.

Li H.-C., Lee Z.-H., Wana N.-J., Shen C.-C., Li T.-Y., Yuan D.-X., Chen Y.-H. (2011) The $\delta^{18}O$ and $\delta^{13}C$ records in an aragonite stalagmite from Furong Cave, Chongqing, China: A-2000-year record of monsoonal climate. *J. Asian Earth Sci.*, **40**, 1121–1130.

Lorens R.B. (1981) Sr, Cd, Mn, and Co distribution coefficients in calcite as a function of calcite precipitation rate. *Geochim. Cosmochim. Acta*, **45**, 553-561.

Möller P. and Parekh P.P. (1966) Influence of magnesium on the ion-activity product of calcium and carbonate dissolved in seawater: A new approach. *Mar. Chem.*, **3**, 63–77.

Mucci A. and Morse J.W. (1983) The incorporation of Mg^{2+} and Sr^{2+} into calcite overgrowths: influences of growth rate and solution composition. *Geochim. Cosmochim. Acta*, **47**, 217-233.

Nielsen L.C., DePaolo D.J., and De Yoreo J.J. (2012) Self-consistent ion-by-ion growth model for kinetic isotopic fractionation during calcite precipitation. *Geochim. Cosmochim. Acta*, **86**, 166–181.

O'Neil J.R., Clayton R.N., and Mayeda T.K. (1969) Oxygen isotope fractionation in divalent metal carbonates. *J. Chem. Phys*. **51**, 5547–5558.

Paquette, J. and Reeder, R.J. (1995) Relationship between surface structure, growth mechanism, and trace element incorporation in calcite. *Geochim. Cosmochim. Acta*, **59**, 735-749.

Patterson W. P., Smith G. R., and Lohmann K. C. (1993) Continental paleothermometry and seasonality using the isotopic composition of aragonite otoliths of freshwater fishes. In *Climate Change in Continental Isotopic Records* (eds. P. K. Swart, C. K. Lohmann, J. Mckenzie, and S. Savin), *Geophys. Monogr. Ser.* **78,** 191–202.

Rohl A.L., Wright K., and Gale J.D. (2003) Evidence from surface phonons for the (2x1) reconstruction of the (101–4) surface of calcite from computer simulation. *Am. Mineral. (Letters), **88**, 921–925.*

Rollion-Bard C., Chaussidon M. and France-Lanord C. (2003) pH control on oxygen isotopic composition of symbiotic corals. *Earth Planet. Sci. Lett*., **215**, 275–288.

Rollion-Bard C., Blamart D., Cuif J.-P., and Dauphin Y. (2010) In situ measurements of oxygen isotopic composition in deep-sea coral, Lophelia pertusa: Re-examination of the current geochemical models of biomineralization. *Geochim. Cosmochim. Acta*, **74**, 1338–1349.

Rosenheim B.E., Swart P.K., and Willenz P. (2009) Calibration of sclerosponge oxygen isotope records to temperature using high-resolution $\delta^{18}O$ data. *Geochim. Cosmochim. Acta*, **73**, 5308–5319.

Stipp, S.L.S., Hochella Jr., M.F., Parks, G.A., and Leckie, J.O. (1992) Cd^{2+} uptake by calcite, solid-state diffusion, and the formation of solid-solution: Interface process observed with near-surface sensitive techniques (XPS, LEED, and AES). *Geochim. Cosmochim. Acta*, **56**, 1941-1954.

Stipp S.L.S. (1999) Toward a conceptual model of the calcite surface: Hydration, hydrolysis, and surface potential. *Geochim. Cosmochim. Acta*, **63,** 3121–3131.

Stoll H.M., Rosenthal Y., and Falkowski P. (2002) Climate proxies from Sr/Ca of coccolith calcite: Calibrations from continuous culture of *Emiliania huxleyi. Geochim. Cosmochim. Acta*, **66**, 927–936.

Tang J., Köhler, S.J., and Dietzel, M. (2008a) Sr^{2+}/Ca^{2+} and $^{44}Ca/^{40}Ca$ fractionation during inorganic calcite formation: I. Sr incorporation. *Geochim. Cosmochim. Acta*, **72**, 3718-3732.

Tang J., Dietzel M., Bohm F., Kohler S.J., and Eisenhauer A. (2008b) Sr^{2+}/Ca^{2+} and $^{44}Ca/^{40}Ca$ fractionation during inorganic calcite formation: II. Ca isotopes. *Geochim. Cosmochim. Acta*, **72**, 3733-3745.

Tarutani T., Clayton R.N., and Mayeda T.K. (1969) The effects of polymorphism and magnesium substitution on oxygen isotope fractionation between calcium carbonate and water. *Geochim. Cosmochim. Acta* **33**, 986–996.

Tesoriero A.J. and Pankow J.F. (1996) Solid solution partition of Sr^{2+}, Ba^{2+}, and Cd^{2+} to calcite. *Geochim. Cosmochim. Acta*, **60**, 1053-1063.

Thorrold S. R., Campana S. E., Jones C. M., and Swart P. K. (1997) Factors determining $\delta^{13}C$ and $\delta^{18}O$ fractionation in aragonitic otoliths of marine fish. *Geochim. Cosmochim. Acta* **61,** 2909–2919.

Tseng W.-N., Chang C.W., Wang C.-H., Shiao J.-C., Iizuka Y., Yang Y.-J., You C.F., Ložys L. (2007) Misidentification of the migratory history of anguillid eels by Sr/Ca ratios of vaterite otoliths. *Mar. Ecol. Prog. Series* **348**, 285–295.

Urey H. C. (1947) The thermodynamic properties of isotopic substances. *J. Chem Soc.* 562–581.

Usdowski E. and Hoefs J. (1993) Oxygen isotope exchange between carbonic acid, bicarbonate, carbonate, and water: a re-examination of the data of McCrea (1950) and an expression for the overall partitioning of oxygen isotopes between the carbonate species and water. *Geochim. Cosmochim. Acta*, **57**, 3815–3818.

van Cappellen P., Charlet L., Stumm W., and Wersin P. (1993) A surface complexion model of the carbonate mineral-aqueous solution interface. *Geochim. Cosmochim. Acta*, **57,** 3505–3518.

Watanabe T., Gagan M.K., Corrége T., Scott-Gagan H., Cowley J., and Hantoro W.S. (2003) Oxygen isotope systematics in *Diploastrea heliopora*: new coral archive of tropical paleoclimate. *Geochim. Cosmochim. Acta*, **67**, 1349–1358.

Watson, E.B. and Liang, Y. (1995) A simple model for sector zoning in slowly growing crystals: Implications for growth rate and lattice diffusion, with emphasis on accessory minerals in crustal rocks. *Am. Mineral.*, **80**, 1179-1187.

Watson, E.B. (1996) Surface enrichment and trace-element uptake during crystal growth. *Geochim. Cosmochim. Acta*, **60**, 5013-5020.

Watson, E.B. (2004) A conceptual model for near-surface kinetic controls on the trace-element and stable isotope composition of abiogenic calcite crystals. *Geochim. Cosmochim. Acta*, **68**, 1473-1488.

White, R.M.P., Dennis, P.F., Atkinson, 1043 T.C. (1999) Experimental calibration and field investigation of the oxygen isotopic fractionation between biogenic aragonite and water. *Rapid Commun. Mass Spetrcom.*, **13**, 1242–1247.

Wyndham T., McCulloch M., Fallon S., and Alibert C. (2004) High-resolution coral records of rare earth elements in coastal seawater: Biogeochemical cycling and a new environmental proxy. *Geochim. Cosmochim. Acta*, **68**, 2067–2080.

Zheng Y.-F. (1999) Oxygen isotope fractionation in carbonate and sulfate minerals. *Geochem. J.*, 33, 109–126.

Zhou G.T. and Zheng Y.-F. (2003). An experimental study of oxygen isotope fractionation between inorganically precipitated aragonite and water at low temperatures. *Geochim. Cosmochim. Acta*, **67**, 387–399.

Figure Captions

Figure 1. a) pH values (NBS scale) recorded during whole experiment (A) and during aragonite crystallization (B).

Figure 2. Reflected (A) and transmitted (B) light images of aragonite spherulites. A) Burn marks are from oxygen isotope analyses with 20-30 μm beam (session-3), REE labels and arrows indicate where REE spikes were detected in session-2.

Figure 3. $10^3 \cdot \ln(\alpha^{18}O)$ versus aragonite growth rate. $10^3 \cdot \ln(\alpha^{18}O)$ error bars are internal (n=1) or external (n>1) standard error at 1σ level. a) Here the data are without estimation of V error; contours mark adjacent data points, which are averaged on Figure 3b. b) V error bars of these averaged data were calculated as 1 s.e. of the multiple measurements presented on Figure 3a.

Figure 4. Comparison with literature data for calcite. The same data as on Figure 3b together with the values of $10^3 \cdot \ln(\alpha^{18}O)$ between calcite and fluid reported in previous studies. Here calcite precipitated at 24.6±0.1°C and pH=8.1±0.1 (Gabitov et al. 2012) and 25°C and pH=8.3 (Dietzel et al. 2009). Curves are GEM simulations at three values of D_s=0.01, 0.06, and 0.2 nm^2/s. Fractionation factors of aragonite-fluid and CO_3^{2-}-fluid are from Kim et al. (2006).

Figure S-1. Evaluation of spherulite growth rate using analytical spot profiles. See Appendix-2 for details.

Table 1. Composition of the sampled fluids from which aragonite grew.

sub-sample	t hr	pH_{NBS}	$\delta^{18}O_{SMOW}$ ‰
Initial	-209	5.94	-10.63
Prior nucleation	-26	8.18	n/a
Sm-spike	0	8.37	-9.07
La-spike	5	8.36	-9.08
Nd-spike	32	8.42	n/a
Tb-spike	129	8.59	-8.93
Final	215	8.62	-8.39

Initial fluid was not exposed to CO_2 atmosphere.
pH and $\delta^{18}O_{SMOW}$ of the fluid at the onset of crystallization were estimated to be 8.27±0.09 and -9.85±0.78 ‰.
t is the time of crystallization from the addition of Sm spike. Initial time was estimated as 209 hours prior Sm addition by visual monitoring of the experimental flask with naked eye every 12-24 hours. The onset of aragonite precipitation was estimated as 13 hours prior to addition of Sm.
Sm, La, Nd, and Tb correspond to the fluid sub-sample collected immediately after addition of REE.
Finnigan MAT 251 IRMS 1σ=0.08 ‰ for $\delta^{18}O_{SMOW}$.

Table 2. Fractionation factors of $^{18}O/^{16}O$ within aragonite spherulites.
SIMS profiles within spherulites.

L (μm)	$10^3 \cdot \ln(\alpha^{18}O)$ (‰)	s.e.
Profile-1 (edge-edge), 10-15 μm beam		
10	27.61	0.47
25	25.55	0.52
45	24.39	0.44
62	24.37	0.47
80	25.65	0.89
100	26.75	0.38
Profile-2 (edge-center), 10-15 μm beam		
20	27.93	0.55
56	26.20	0.38
74	25.66	0.51
91	25.96	0.41
Profile-3 (edge-center), 10-15 μm beam		
10	28.49	0.40
36	25.71	0.65
51	25.35	0.36
62	25.12	0.48
Profile-4 (edge-edge), 20-30 μm beam		
30	26.19	0.32
65	25.45	0.54
100	26.66	0.30
Profile-5 (edge-center), 20-30 μm beam		
35	26.51	0.33
65	25.89	0.85
100	25.77	0.86
Profile-6 (edge-center), 20-30 μm beam		
25	27.20	0.32
55	25.09	0.34
85	25.77	0.86

SIMS analyses were performed as profiles between the edges of the crystals. For example distance L of 25 and 1467 μm corresponds to the opposite edges of the crystal, i.e. start and end of analytical profile.
$\alpha^{18}O=(^{18}O/^{16}O)_{calcite}/(^{18}O/^{16}O)_{fluid}$, where $(^{18}O/^{16}O)_{fluid}=0.0019841$.
s.e.=s.d./√n.
10-15 μm ion beam was used in analytical session-1; 20-30 μm beam – in session-2.

Table 3. Mean fractionation factors of $^{18}O/^{16}O$ in each REE-spiked zone of aragonite spherulites.

REE	V±s.e. (nm/s)	$10^3 \cdot \ln(\alpha^{18}O)$ (‰)	s.e.	n
		Before data averaging (Figure 3a)		
Nd-Tb	0.0433	27.61	0.47	1
Sm-Nd	0.1709	27.53	0.52	5
Sm-Nd	0.0850	28.49	0.40	1
Prior Sm	≥0.5880 *	26.21	0.43	7
Sm-La	1.1690	25.09	0.34	1
La-Nd	0.2000	26.51	0.33	1
La-Nd	0.3500	27.20	0.32	1
		After data averaging (Figure 3b and 4)		
	0.0641±0.0209	28.14	0.22	2
	0.1710±0.0855	27.53	0.52	5
	0.2750±0.0750	26.86	0.34	2
	0.8788±0.2908	25.65	0.56	8

REE shows the aragonite zone grew between additions of two REE spikes. For example Nd-Tb means that growth rate and fractionation factor presented in this row were determined in the aragonite grown between addition of Nd and Tb spikes. The error at 1σ level is the standard error of $10^3 \cdot \ln(\alpha^{18}O)$ from the single or multiple spots in each REE spiked zone.
n is the number of SIMS analytical spots which yielded n number of $10^3 \cdot \ln(\alpha^{18}O)$ values, but not the number of V, which is equal to two for the averaged data.
(*) - Growth rates from "prior Sm" zones were estimated from the time between the absence of crystallization and when crystals became observable in the flask (addition of Sm spike).

Table S-1. SIMS $\delta^{18}O_{VPDB}$, ^{42}Ca and REE intensities and from analytical sessions 2 and 3. ^{42}Ca and REE were determined on the top of the burn marks from oxygen isotope session-3.

L μm	$^{139}La/^{42}Ca$ x 1e+5	s.e.	$^{143}Nd/^{42}Ca$ x 1e+5	s.e.	$^{149}Sm/^{42}Ca$ x 1e+5	s.e.	$^{159}Tb/^{42}Ca$ x 1e+5	s.e.	$\delta^{18}O_{VPDB}$	s.e.
					Profile-4 (edge-edge)					
30	500	8.00	2.18	0.827	161	4.47	0.404	0.280	-13.26	0.32
65	22.8	2.62	2.88	0.627	16.3	2.57	0.460	0.250	-14.32	0.32
100	246	5.66	3.30	0.648	166	8.60	0.166	0.166	-12.72	0.29
					Profile-5 (edge-edge)					
35	520	13.8	2.73	0.570	108	5.22	0.402	0.313	-12.87	0.32
65	9.16	1.12	2.31	0.561	16.8	4.79	0.722	0.393	-14.32	0.32
100	12.3	1.26	2.03	0.945	22.4	5.24	0.813	0.324	-14.46	0.33
					Profile-6 (edge-edge)					
25	1017	29.5	9.6	1.07	307	11.1	2.46	0.790	-12.19	0.31
55	7.84	1.00	1.27	0.495	16	1.68	1.19	0.640	-14.32	0.33
85	12.3	1.26	2.03	0.945	22	5.24	0.813	0.324	-14.46	0.33

Figure 1. pH during aragonite crystallization

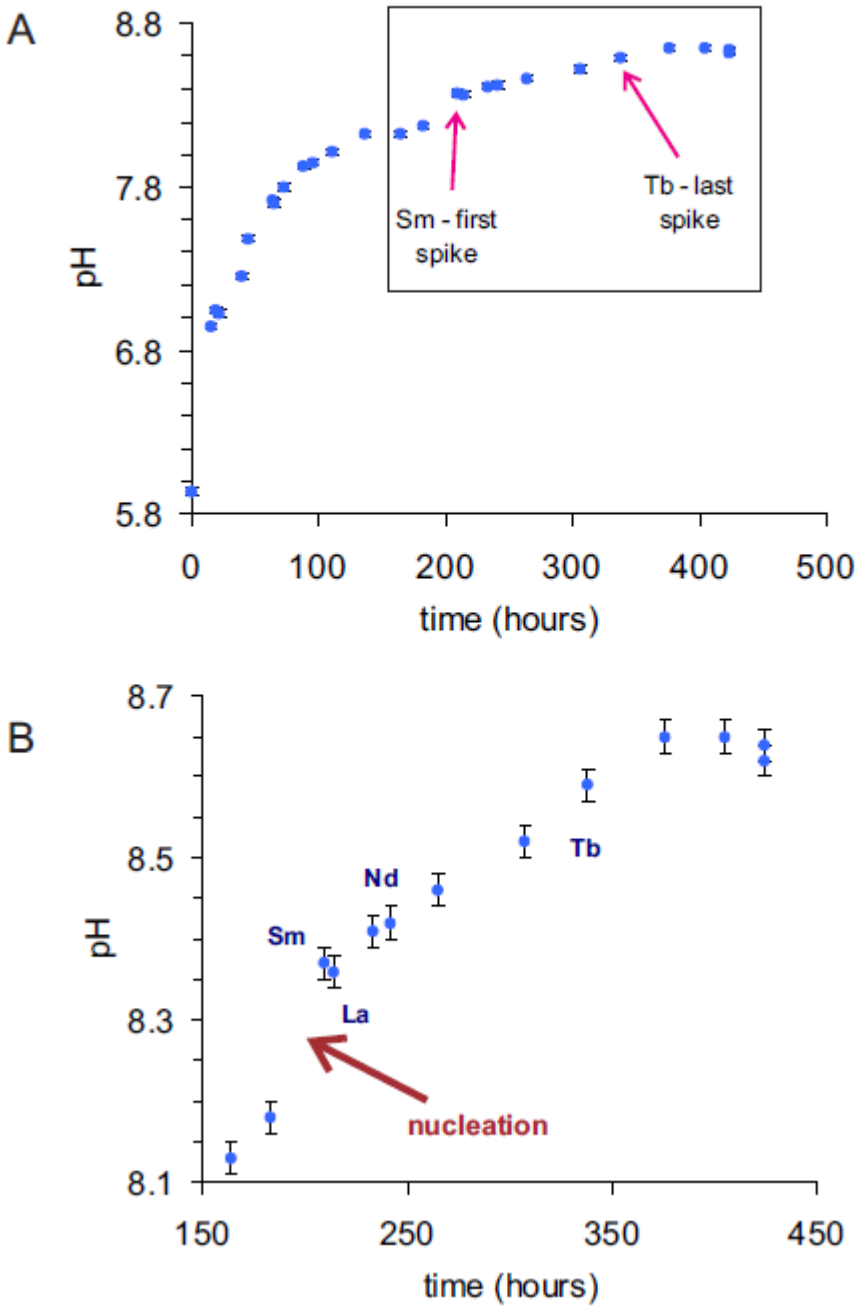

Figure 2. Aragonite spherulites.

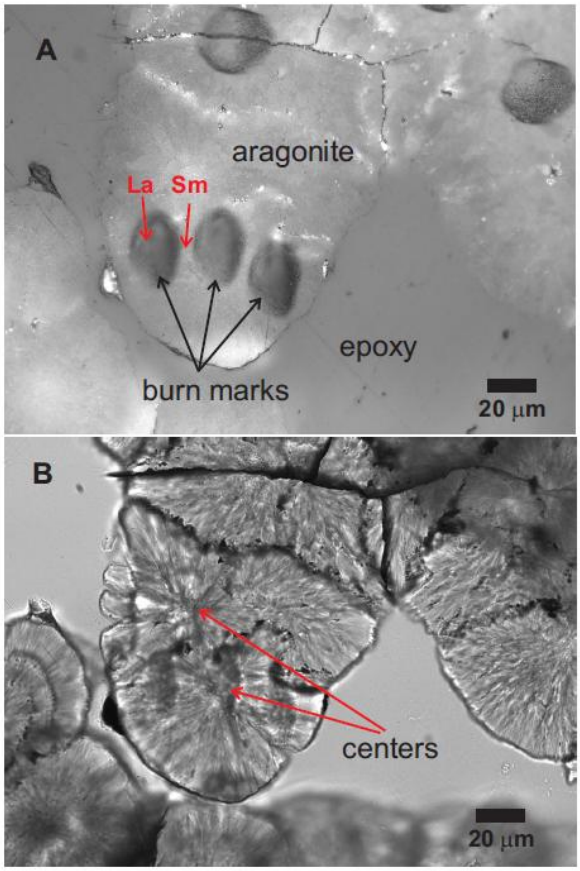

Figure 3. Fractionation factor versus aragonite growth rate

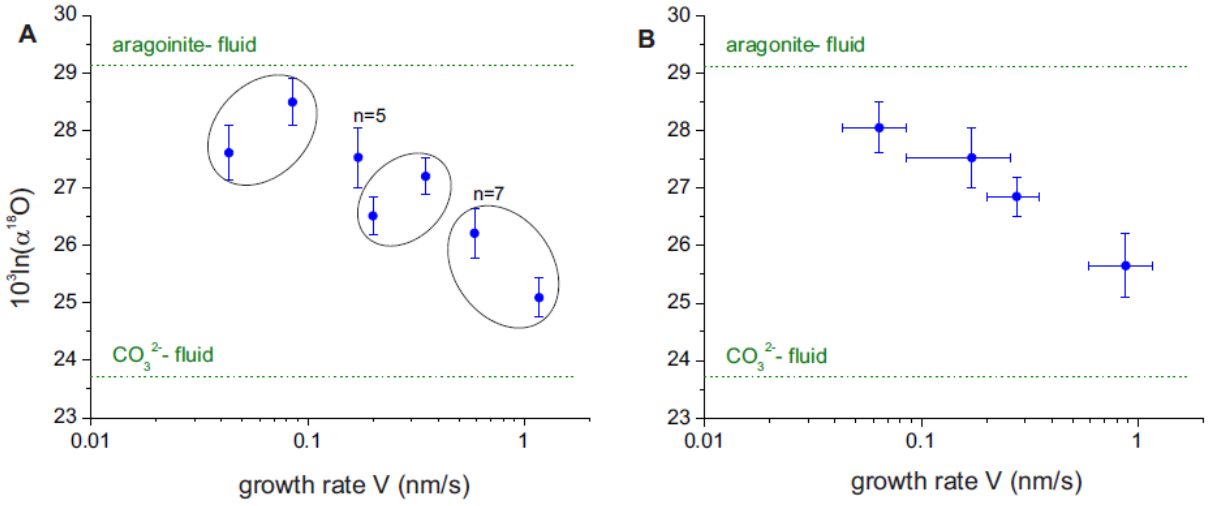

Figure 4. Comparison of aragonite and calcite data

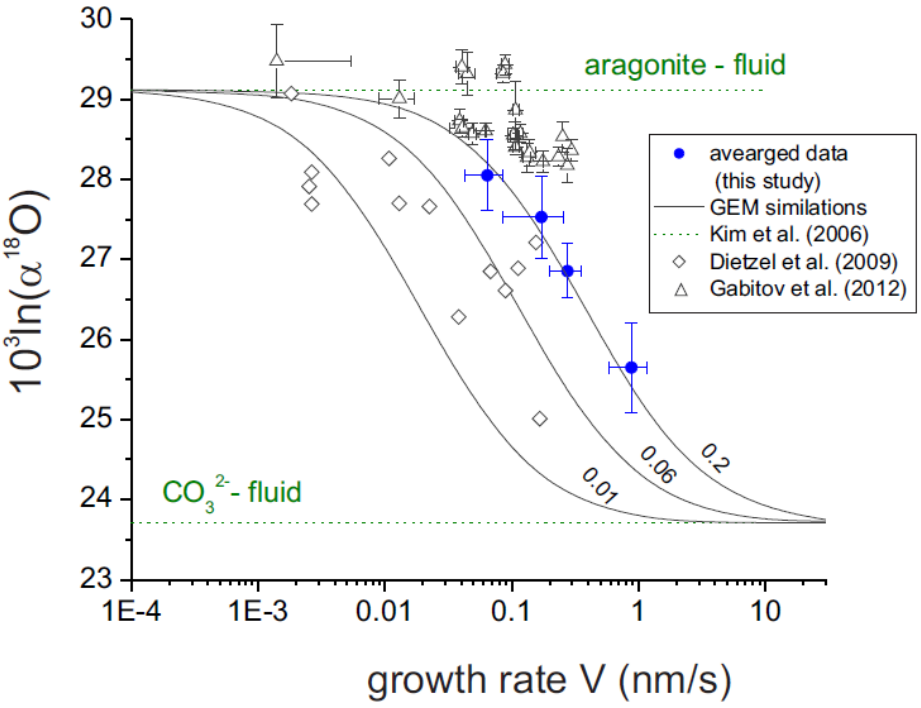

Figure S-1. An example of growth rate evaluation.

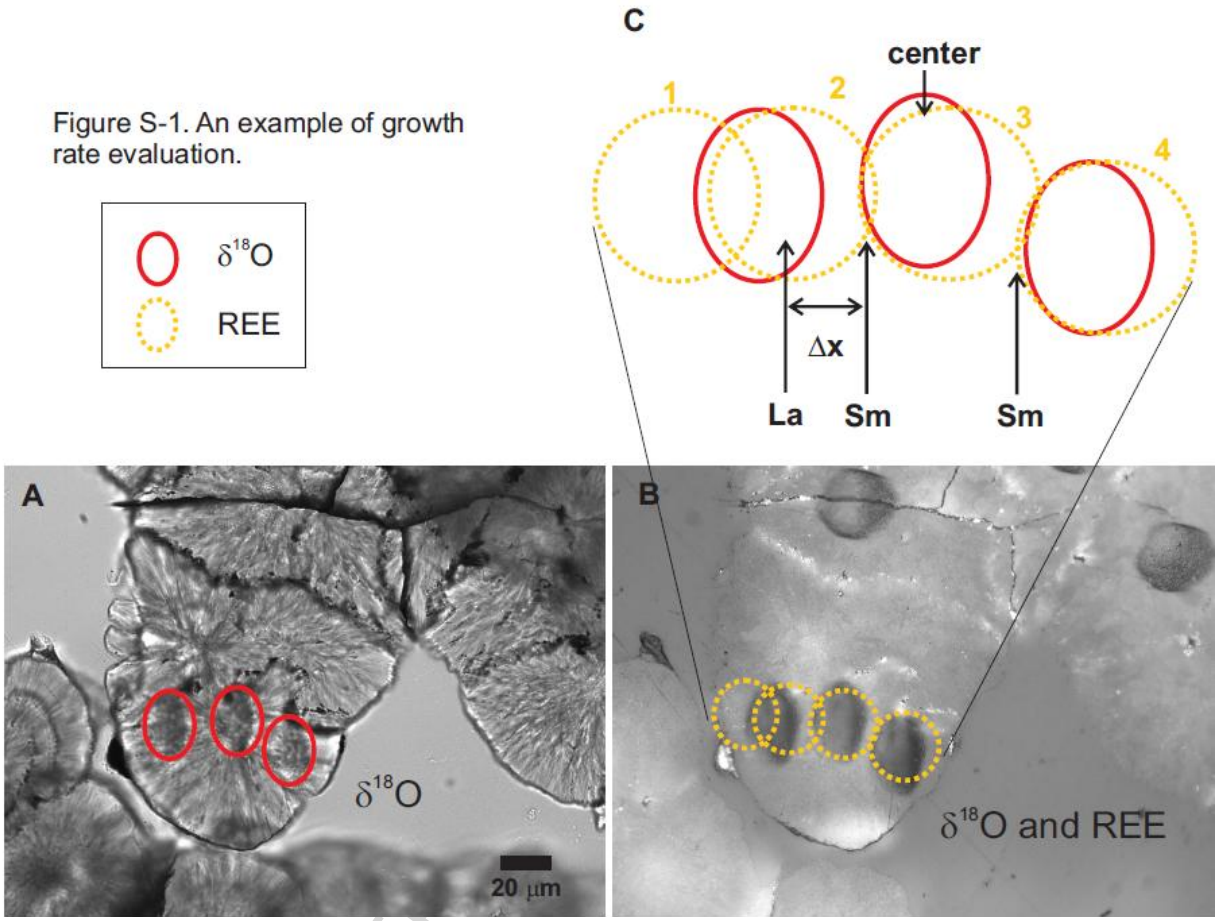

Highlights

> Hemispherical bundles of aragonite crystals were grown from aqueous solution under controlled conditions
> Intraspherulite SIMS analyses revealed core-to-rim changes in $\alpha^{18}O_{aragonite\text{-}fluid}$
> $\alpha^{18}O_{aragonite\text{-}fluid}$ decreases with increasing growth rate
> $\alpha^{18}O_{aragonite\text{-}fluid}$ approaches $\alpha^{18}O_{eq(CO_3^{2-}\text{-}fluid)}$ at high growth rate